

Crustal structure in the Binchuan basin of Yunnan constrained from receiver functions on a 2-D seismic dense array*

Xiaohuan Jiang¹ Hongfeng Yang^{2,✉} Wei Yang³ Weitao Wang³

¹ Shenzhen Research Institute, The Chinese University of Hong Kong, Shenzhen, Guangdong 518057, China

² Earth System Science Programme, Faculty of Science, The Chinese University of Hong Kong, Hong Kong 999077, China

³ Institute of Geophysics, China Earthquake Administration, Beijing 100081, China

Abstract The Binchuan region is located in a seismically active area in northwestern Yunnan, China. The detailed crustal structure is important to understand the tectonic evolution and to assess the seismic hazard in the study area. With a 2-D dense array deployed in this region, we use teleseismic receiver function traditional imaging methods, including the $H\text{-}\kappa$ and common-conversion-point stacking methods, to derive high-resolution crustal thickness and v_p/v_s ratio maps. Our results indicate that the crustal thickness increases from ~40 km to ~46 km in the south-north direction, and the average crustal thickness beneath the Binchuan basin is ~42 km. Our results agree with previous results but have higher resolution due to dense interstation spacing.

Keywords: Binchuan region; crustal thickness; receiver function; $H\text{-}\kappa$ stacking; common-conversion-point stacking

1 Introduction

Since ~45 Ma, the collision of the Indian and Eurasian plates has generated the general north-south (N-S) directional shortening and east-west (E-W) directional extension in the Tibetan Plateau (TP), resulting in the dramatic uplift and thickening of the underlying crust (e.g. Yin and Harrison, 2000; Li et al., 2015; Hu and Yao, 2018). The Yunnan Province of southwestern China is located in the southeastern margin of the TP and has a complicated tectonic environment. Several well-known north-south (N-S) oriented faults were formed in Yunnan,

producing damaging historic earthquakes (e.g. Huang et al., 2018; Yang et al., 2020). The Binchuan basin (BCB), the second largest basin in northwestern Yunnan, is mainly controlled by the Chenghai fault (CHF). The CHF orients nearly in the N-S direction, with a length of 200 km, starting from Yongsheng in the north and intersecting with the northwest-southeast (NW-SE) trending Red River fault (RRF) in the south (Figure 1a). The largest earthquake that occurred in this area is the 1515 $M_{\text{7}}\frac{1}{4}$ Yongsheng earthquake (e.g. Zhou et al., 2004; Wang et al., 2015a) and the latest moderate earthquake, recorded by the China Earthquake Networks Center (CENC), is the M_{W} 4.9 earthquake occurred on 21 July 2019 at Yongsheng. A recent study indicates that the seismicity along the CHF is mainly strikeslip, and concentrating in the northern segment (Xu et al., 2020). There are also possibilities of earthquakes in the southern segment of the CHF since there is a ‘seismic gap’ in the study region (Huang et al., 2018; Yang et al., 2020) (Figure 1a). A high-resolution crustal image beneath this region is important to better understand its seismicity distribution and to assess the potential seismic hazard.

From the mid-1980s, many seismic studies have been conducted in the Yunnan area, such as active seismic exploration (e.g. Kan et al., 1986; Bai and Wang, 2004; Wang et al., 2015b; Chen et al., 2016), teleseismic receiver function inversion (e.g. Hu et al., 2005; Wang et al., 2010; Bai et al., 2018), and body wave and surface-wave tomography (e.g. Huang et al., 2002, 2012, 2015; He et al., 2004; Yao et al., 2006, 2008; Chen et al., 2018). All these studies had limited lateral resolutions, due to the relatively sparse station distribution. During recent decades, with the development of seismographs techniques, more dense seismic arrays are deployed to make it possible to obtain 3-D high-resolution underground structures (e.g. Schmandt

* Received 29 August 2020; accepted in revised form 3 December 2020; published 28 December 2020.

✉ Corresponding author. e-mail: hyang@cuhk.edu.hk

© The Seismological Society of China and Institute of Geophysics, China Earthquake Administration 2020

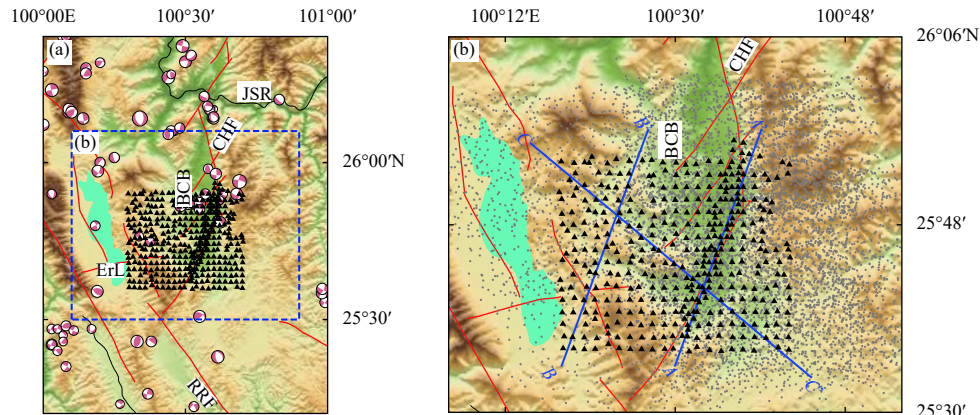


Figure 1 (a) Location and faults (red lines) in the study region. JSR: Jinsha river, ErL: Erhai lake, BCB: Binchuan basin, CHF: Chenghai fault, RRF: Red-River fault. Black solid triangles denote stations. Beach balls represent moment tensor solutions from Xu et al. (2020); (b) 2-D dense array with 381 short-period seismometers (black solid triangles). Gray dots denote Ps piercing points for CCP stacking. AA', BB' and CC' are three profiles used in Section 3.3 for CCP stacking

and Clayton, 2013; Lin et al., 2013; Inbal et al., 2015; Jiang et al., 2019). To delineate fault zone structures and track temporal changes around the faults, we have deployed multi-scale dense arrays in the Binchuan area in the past few years. The first 2-D dense array was deployed in the field for three months in 2017 and consisted of 381 intermediate-period three-component seismometers with an average interstation spacing of ~2 km. In 2018, we deployed two other linear arrays (8-km and 5-km long) using the same instruments with much smaller interstation spacing, e.g. 30–50 m, across the southern branch of the CHF. With numerous local and teleseismic earthquakes recorded by the dense arrays, there have been numerous results using different methods. For instance, by analyzing the earthquake surface wave and ambient noise cross-correlation functions (NCFs), Xu et al. (2018) concluded that the dense array is capable to capture geological related features in the Binchuan basin; She et al. (2019) used beamforming analysis and polarization analysis to investigate the characteristics of seismic wave propagation; Zhang et al. (2020) applied body wave tomography method and seismic relocation to obtain the upper crustal velocity structure in the Binchuan area; Yang et al. (2020) used teleseismic travel time and ambient noise tomography to obtain the width and depth extent of the low-velocity zone (LVZ) beneath the CHF with the linear array across the fault.

The teleseismic receiver function (RF) technique is an effective tool to image crustal structure. It removes the effects of the earthquake source and wave propagation outside the study region in recorded three-component P-wave waveform by deconvolving the waveforms on the vertical component from the radial component (e.g. Vinnik, 1977; Langston, 1979). There are many frequently

used RF methods to derive crustal images. For instance, Zhu and Kanamori (2000) developed a $H\text{-}\kappa$ stacking method for individual stations, which does not require to pick phases travel time and can obtain optimum crustal thickness (H) and v_p/v_s ratio (κ) by stacking RFs from all azimuths; Zhu (2000) developed the common-conversion-point (CCP) stacking method which first back-projects RF amplitudes to their P-to-S conversion points using a 1-D background velocity model and then stacks them in the depth domain. A similar method was also developed by Kosarev et al. (1999). Recently, many new array-based techniques have also been developed to image crustal discontinuities using RFs (e.g. Chen et al., 2005; Shang et al., 2012; Li et al., 2018; Jiang et al., 2019).

In this study, our purpose is to obtain high-resolution crustal thickness variation in the Binchuan region using teleseismic receiver function methods. Here we used a 2-D dense array with interstation spacing of ~2 km in the Binchuan area to determine crustal depths variation. In detail, we used the $H\text{-}\kappa$ stacking method to obtain crustal thickness and v_p/v_s ratio for individual stations. Then we applied the CCP stacking method, with the 1-D model beneath every station from the $H\text{-}\kappa$ results as a constraint, to derive detailed crustal thickness variation in the study area.

2 Data

To obtain a high-resolution crustal structure in the Binchuan study area, a dense seismic array was deployed from March 21 to May 30, 2017, by the China Earthquake Administration (CEA) in the southern segment of the Binchuan region (Figure 1a) (e.g. Wang et al., 2018; Xu et

al., 2018; Zhang et al., 2020; Yang et al., 2021). The dense array is a $30\text{ km} \times 40\text{ km}$ area and contains total 381 short-period seismometers (types: EPS, EPS-2 and QS-5A) in the frequency band 5–150 Hz with $\sim 2\text{ km}$ spacing.

We used the standard RF technique to process the waveforms. All the vertical-component waveforms were visually inspected to ensure good signal-to-noise ratios by discarding noisy events. After the inspection, we removed linear trends in the waveform data and resampled them to 10 Hz. A band-pass filter from 0.05 Hz to 2 Hz was applied. We selected 111 earthquakes of magnitudes larger than 5 at epicentral distance ranging 30° – 95° for this study (Figure 2). Most of their magnitudes were between 5.0 and 5.5, and only 10 earthquakes had magnitudes larger than 6.0 (Figure 2). Figure 3 gives examples of 4 earthquakes with different back-azimuths and magnitudes. Here we only exhibited stations along the profile CC' in Figure 1b. Three-component waveforms in Figure 3 have high signal-noise ratio (SNR) and good coherence, which provides the foundation for the follow-up process.

We used three-component P-wave waveforms (50 s before the direct P arrival and 150 s after) to calculate teleseismic RF at each station, using a time domain iteration deconvolution method (Ligorria and Ammon, 1999). A Gaussian low-pass filter of 1 Hz was applied to suppress high-frequency noise in RF waveforms. For each station, all receiver functions were sorted by back-azimuth and inspected. We manually removed bad receiver func-

tions with poor coherence. As a result, we obtained 11128 high-quality receiver functions. Receiver functions with similar back-azimuths and ray-parameters were stacked to remove clustered events (Figure 4). These calculated RFs were then used to study the crustal structure of the study area.

3 Data analysis

3.1 H - κ stacking

Firstly we applied the H - κ stacking method (Zhu and Kanamori, 2000) to estimate crustal thickness H and v_p/v_s ratio κ underneath each station. To reduce the trade-off between H and κ , the method uses the time delays of P-to-S converted phase Ps and its crustal multiple phases PpPs and PpSs + PsPs from Moho to simultaneously determine these two parameters. In this study, we set weighting factors to be 0.6, 0.3 and 0.1 for the three phases, respectively, in the data stacking and used a crustal reference P-wave velocity of 6.3 km/s.

Receiver functions of 6 stations and their H - κ stacking results are shown in Figure 4. For the stations in the mountains area (such as 033, 092, 176 and 226 in Figure 4), corresponding RFs have clear Moho Ps and their multiples. In contrast, RFs recorded by stations in the Binchuan basin (such as 016 and 058 in Figure 4) are

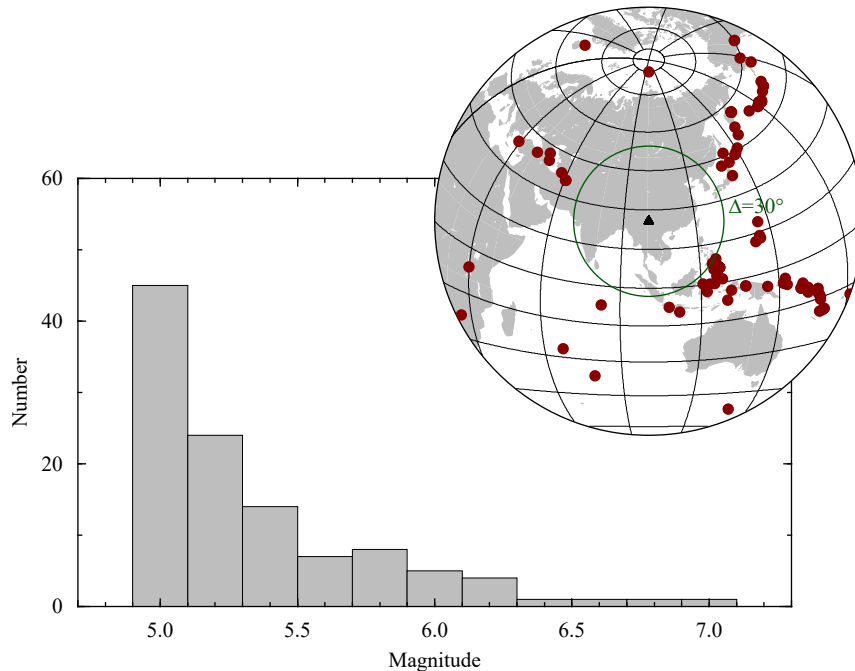


Figure 2 Distribution of magnitudes and locations of 111 teleseismic earthquakes (red dots) with magnitudes larger than 5 in the epicentral distance ranging 30° – 95° , the black triangles denote station locations

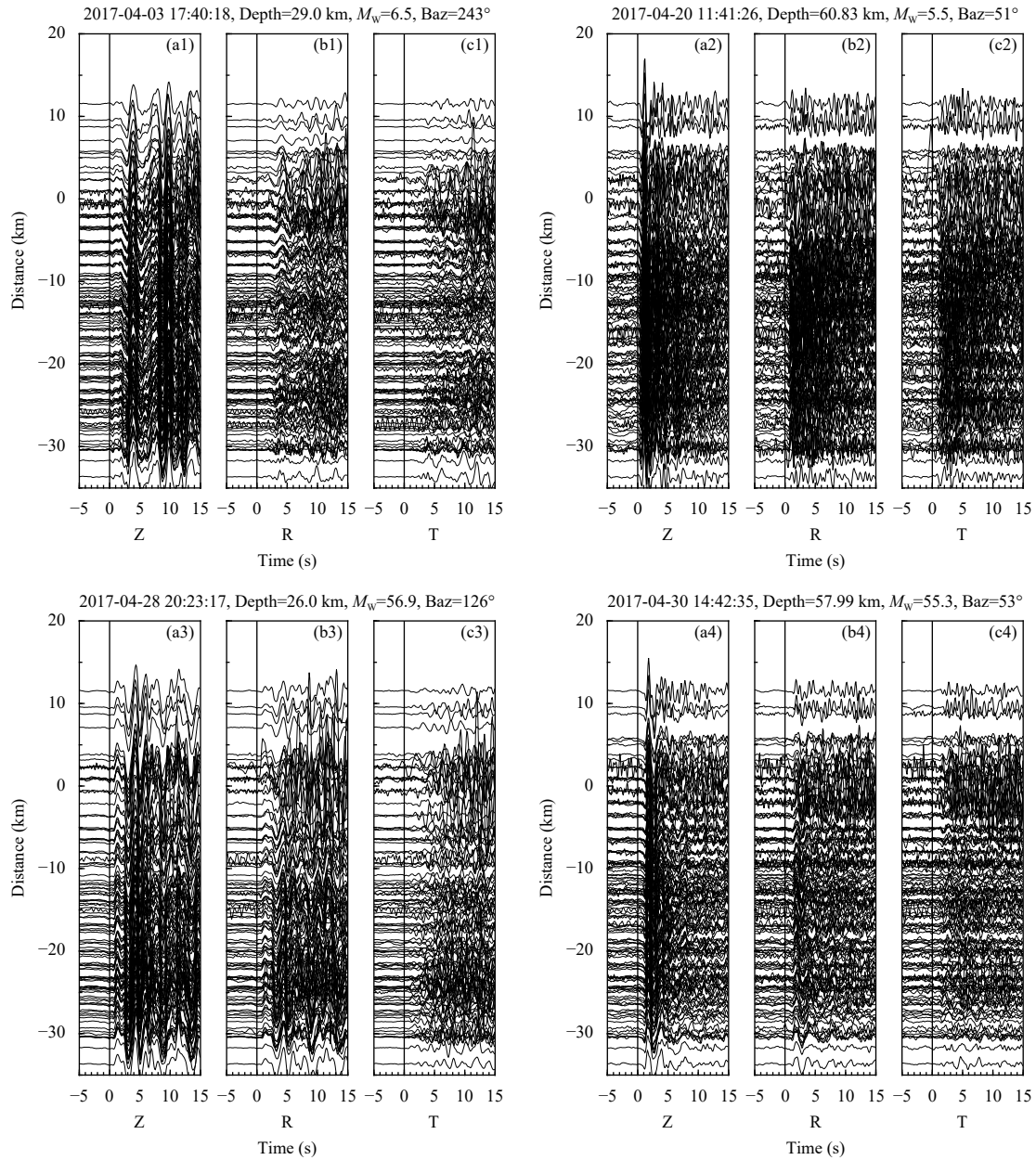


Figure 3 Teleseismic waveforms of vertical (Z) (a1, a2, a3, a4), radial (R) (b1, b2, b3, b4) and tangential (T) (c1, c2, c3, c4) components for 4 earthquakes aligned with the first P arrival with stations along with the profile CC' in Figure 1b

affected by multiples caused by shallow low-velocity sediment, and the Moho phases cannot be distinguished well. Although a variety of teleseismic techniques have been proposed and developed to determine both the sedimentary and crustal structures (e.g. [Yeck et al., 2013](#); [Tao et al., 2014](#); [Yu et al., 2015](#); [Cunningham and Lekic, 2019](#)), here we only applied $H\text{-}\kappa$ method to 148 stations outside the Binchuan basin. Receiver functions of most stations have weak but identifiable PpPs phase, which allows us to constrain the crustal v_p/v_s ratios to be between 1.5 and 1.9 and crustal thicknesses between 34 km and 55 km for the area outside the BCB. [Zhang et al. \(2020\)](#) used

an improved 1-D seismic velocity model method ([Matrullo et al., 2013](#)) with the arrival time differentials to obtain an average v_p/v_s of 1.72 in this area. With the average v_p/v_s , [Zhang et al. \(2020\)](#) conducted a travel time tomography using local earthquake data to derive P-wave velocity model. The average v_p/v_s from our $H\text{-}\kappa$ result is ~1.75, which is slightly larger than the result in [Zhang et al. \(2020\)](#).

3.2 CCP stacking

Because the $H\text{-}\kappa$ stacking method stacks receiver functions of all azimuths at a single station, its lateral

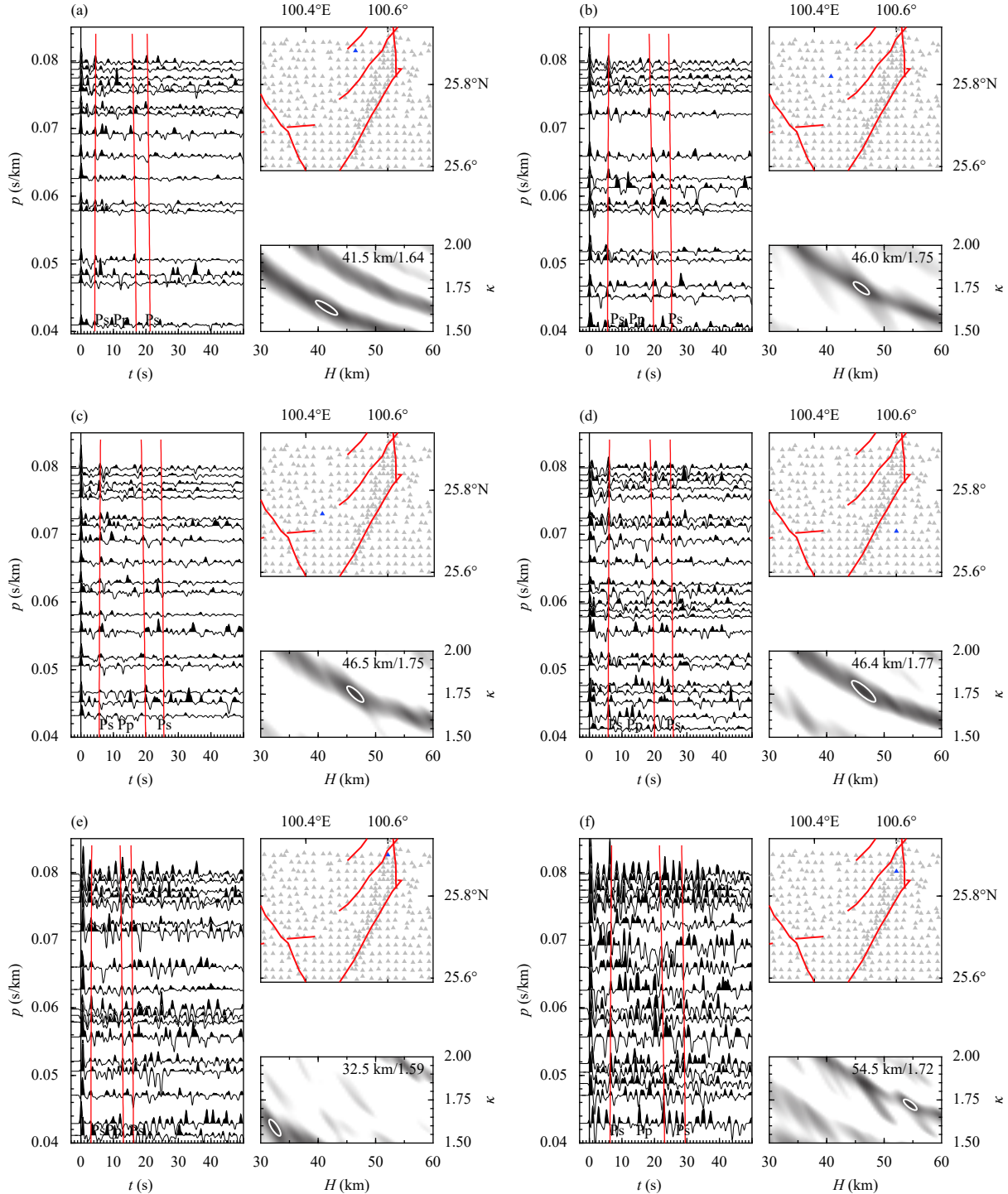


Figure 4 Receiver functions and H - κ stacking results of 6 example stations. Their station names are labeled with 033 (a), 092 (b), 176 (c), 226 (d), 016 (e) and 058 (f). Blue triangles denote the location of the stations. Red lines in the right top panel of figures denote the faults, and the values in the right bottom of figures are optimal crustal thickness and v_p/v_S . The ellipses indicate the best estimates of H and κ and their uncertainties. The red lines are predicted arrival times of Moho Ps and its crustal multiples using the estimated H and κ values

resolution is limited by the interstation spacing. Next, we used the CCP stacking method of Zhu (2000) to image crustal structure with more detail. Amplitudes of all

receiver functions of stations (black triangles in Figure 1) were back-projected to their P-to-S conversion points (shown as gray dots in Figure 1b) based on their time

delays relative to the direct P arrival. Here we used 1-D IASP91 global model as background velocity model and crustal v_p/v_S ratios beneath individual stations from $H\kappa$ stacking results as a constraint. We then divided the crustal volume into 1-km-wide and 0.5-km-high bins and stacked all receiver function amplitudes in each bin.

For the three cross-sections (AA' , BB' and CC') in Figure 1b, we applied CCP stacking method and obtained underneath crustal structure (Figure 5). The first profile (AA') orients along the CHF, and passes through the BCB. Moho beneath the southwestern (SW) CHF is shallower than the northeastern (NE) part, and ranging from ~40 km to ~45 km (Figure 5). The second profile (BB') is parallel to the AA' profile, but is located in the west with ~20 km to the outside of the BCB. In the CCP results of this profile (Figure 5), crustal depth variation is similar to the result of AA' profile, which is shallower at SW direction and deeper in the NE edge, with the range of ~40 km to ~46 km. The third profile (CC') crosses with the other two profiles and is nearly perpendicular to the CHF orientation (Figure 1b). For this profile, Moho depth varies slightly with an average of ~43 km.

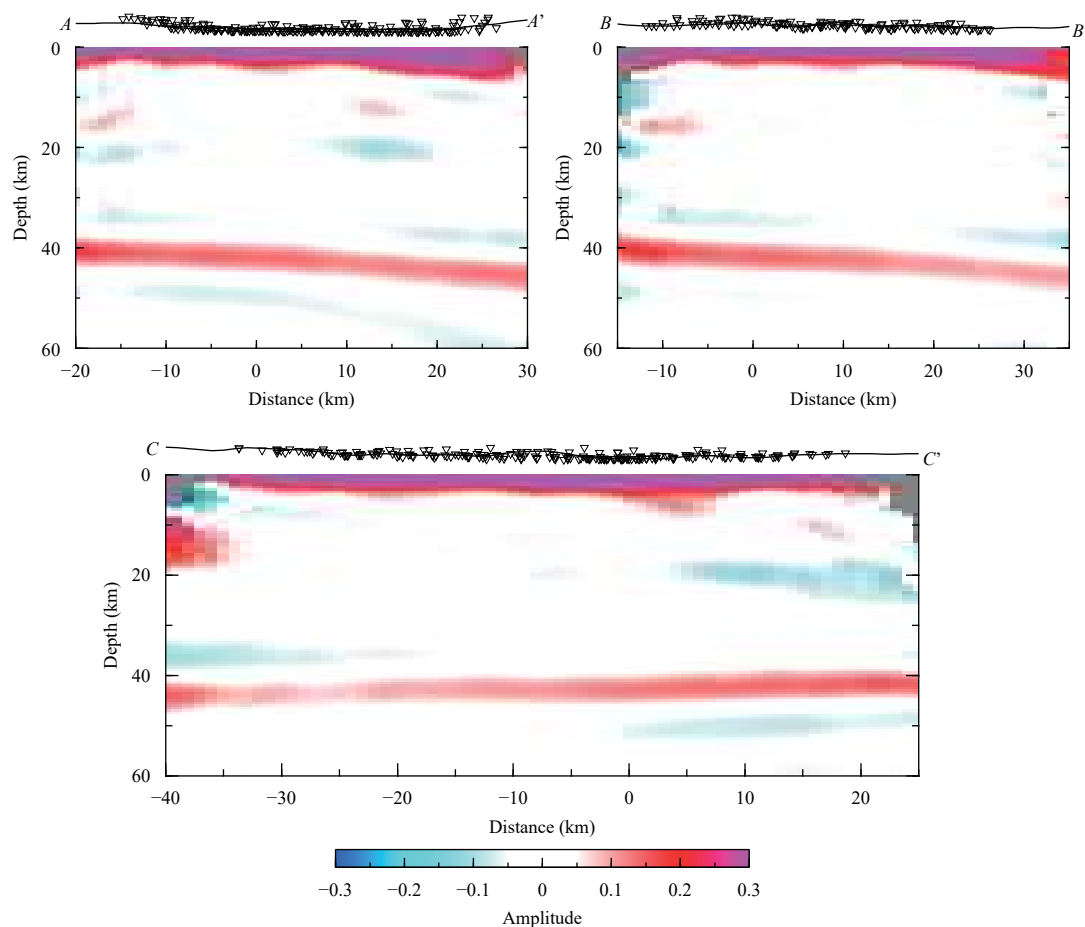


Figure 5 CCP stacking results along with the three profiles (AA' , BB' and CC') in Figure 1b

4 Discussion and conclusions

In the preceding section, we analyzed RFs from the 2-D seismic array using the $H\kappa$ and CCP stacking methods and obtained the crustal depths. To better understand the crustal structure in the whole study area, we set 16 intersected profiles (Figure 6a), then apply the CCP stacking method to obtain crustal depths of every profile. Then we interpolate crustal depths from the CCP stacking results to derive a 2-D image of the Moho depths (Figure 6b). Results indicate that Moho depth is deeper in the northern area than the southern area. The shallowest Moho of ~40 km locates at the southern edge of the CHF, and the deepest depth of ~46 km is in the northeastern outside the BCB.

In this area, there have been other previous results about the Moho depth variation. With 27 seismic stations (interstation spacing ~30 km), Chen et al. (2019) used RF $H\kappa$ method to obtain Moho depths beneath the Binchuan area. The result indicated the Moho depth of the region ranged from 42 km in the south of the Binchuan basin to

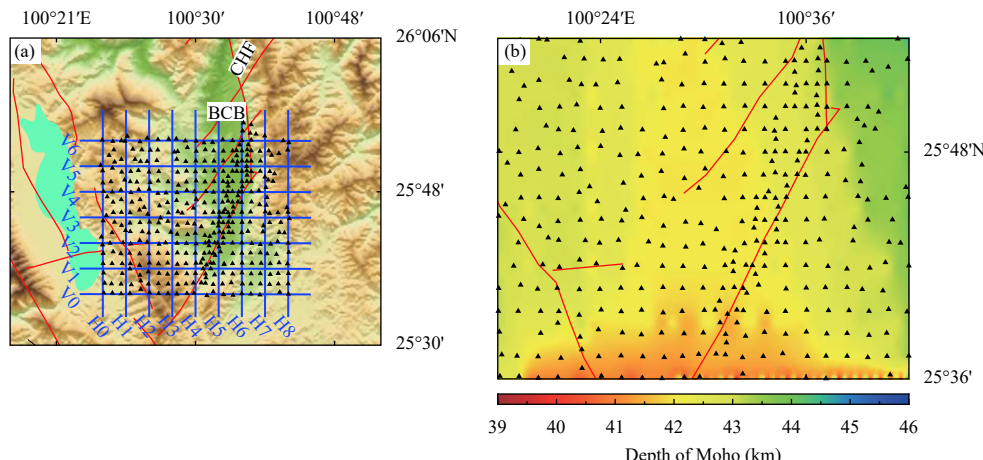


Figure 6 (a) 16 intersected profiles (blue lines) across the 2-D array. Black solid triangles denote stations. BCB: Binchuan basin, CHF: Chenghai fault; (b) Moho depth for the study area by digitizing CCP results along with profiles in (a)

54 km in the north to Ningliang. The average Moho depth for our study area was ~44 km (Chen et al., 2019). Sun (2019) used a 300-km-long near-linear array (south to Yunxian and north to Ninglang) with interstation spacing of 2 km, which passed through our 2-D seismic array, to derive the Moho depths of the whole CHF. From the CCP stacking results, the Moho depths ranged from 40 km beneath the southern segment of the CHF to 50 km for the northern segment (Sun, 2019). Chen et al. (2016) used a near north-to-south directed 300 km long wide-angle reflection/refraction seismic profile from Ninglang to Yunxian, across the Binchuan study field. The result indicated the crustal depth of the profile went deeper in a south-to-north direction, from 45 km to 54 km, while the Moho depth of the Binchuan area is 42–45 km (Chen et al., 2016). In our results (Figure 6b), the crustal depth along the CHF is shallower in the southern part than in the northern part, which has very good coherence with previous results in this area but with higher lateral resolution.

On the other hand, our result (Figure 6b) shows slight changes in Moho depths beneath the Binchuan basin, with an average of ~42 km. This result may contain some uncertainties, mainly from the uncertain 1-D initial velocity models. The traditional $H\text{-}\kappa$ method cannot obtain stable results for stations deployed in the Binchuan basin. As mentioned in Section 3.1, considering the shallow sedimentary effects, there have developed a variety of teleseismic techniques to derive the crustal structures (e.g. Yeck et al., 2013; Tao et al., 2014; Yu et al., 2015; Cunningham and Lekic, 2019). To consider the sediment effect, similar approaches can be conducted for stations within the Binchuan basin in further work.

In summary, we calculated teleseismic P-wave receiver functions of 381 short-period seismometers in the

Binchuan basin, Yunnan Province, and estimated crustal thicknesses of individual stations using the $H\text{-}\kappa$ method. We derived the detailed Moho depths underneath the 2-D array using the CCP stacking method. The result indicates a crustal thickness increases in the south-north direction in the field from 40 km to 46 km.

Acknowledgements

This study is supported by the National Key R&D Program of China (No. 2018YFC1503400), China Earthquake Science Experiment Project, CEA (Nos. 2018CSES0101, 2018CSES0102 and 2019CSES0107), HKSAR Research Grant Council GRF (No.14305617), CUHK Direct Grant from Faculty of Science, National Natural Scientific Foundation of China (Nos. 41974069 and 41790463), Chen Yong Academician Workstation of Yunnan Province in China (No. 2014IC007). We thank two anonymous reviewers for their constructive comments that helped improve the paper.

References

- Bai YM, Ai YS, Jiang MM, He YM and Chen QF (2018) Structure of the mantle transition zone beneath the southeastern Tibetan Plateau revealed by P-wave receiver functions. Chin J Geophys **61**(2): 570–583 (in Chinese with English abstract)
- Bai Z and Wang C (2004) Tomography research of the Zhefang-Binchuan and Menglian-Malong wide-angle seismic profiles in Yunnan province. Chin J Geophys **47**(2): 257–267 (in Chinese with English abstract)
- Chen HP, Li ZW, Chu RS, Xie J, Chong JJ and Ye QD (2018) 3D S-wave velocity and radial anisotropy structure of the crust and uppermost mantle in Yunnan, SE Tibet. Chin J Geophys **61**(8): 3219–3236 (in Chinese with English abstract)

- Chen J, Gao Q, Wang J and Deng JM (2019) Crustal depth and S wave velocity structure in Chenghai fault zone from receiver functions. *Earthquake* **39**(1): 72–80 (in Chinese with English abstract)
- Chen L, Wen LX and Zheng TY (2005) A wave equation migration method for receiver function imaging: 1. theory. *J Geophys Res* **110**: B11309
- Chen SW, Wang BS, Tian X, Wang F, Liu B and Li L (2016) Crustal structure from Yunxian-Ninglang wide-angle seismic reflection and refraction profile in northwestern Yunnan, China. *Seismology and Geology* **38**(1): 91–106 (in Chinese with English abstract)
- Cunningham E and Lekic V (2019) Constraining crustal structure in the presence of sediment: a multiple converted wave approach. *Geophys J Int* **219**: 313–327
- He ZQ, Su W and Ye TL (2004) Seismic tomography of Yunnan region using short-period surface wave phase velocity. *Acta Seismologica Sinica* **17**(6): 642–650
- Hu JE, Su YJ, Zhu XG and Chen Y (2005) S-wave velocity and Poisson's ratio structure of crust in Yunnan and its implication. *Science in China Series D: Earth Science* **48**(2): 210–218
- Hu SQ and Yao HJ (2018) Crustal velocity structure around the eastern Himalayan syntaxis: Implications for the nucleation mechanism of the 2017 $M_{\text{S}}6.9$ Mainling earthquake and regional tectonics. *Tectonophysics* **744**: 1–9
- Huang JL, Zhao DP and Zheng SH (2002) Lithospheric structure and its relationship to seismic and volcanic activity in southwest China. *J Geophys Res* **107**(B10): 2255
- Huang J, Liu XJ, Su YJ and Wang BS (2012) Imaging 3-D crustal P-wave velocity structure of western Yunnan with bulletin data. *Earthq Sci* **25**(2): 151–160
- Huang XJ, Wu ZH, Huang XL and Luo RJ (2018) Tectonic geomorphology constrains on quaternary activity and segmentation along Chenghai-Binchuan Fault Zone in Northwest Yunnan, China. *Earth Science* **43**(12): 4651–4670 (in Chinese with English abstract)
- Huang ZC, Zhao DP and Wang LS (2015) P wave tomography and anisotropy beneath Southeast Asia: insight into mantle dynamics. *J Geophys Res* **120**(7): 5154–5174
- Inbal A, Clayton RW and Ampuero JP (2015) Imaging widespread seismicity at midlower crustal depths beneath Long Beach, CA, with a dense seismic array: Evidence for a depth dependent earthquake size distribution. *Geophys Res Lett* **42**: 6314–6323
- Jiang XH, Zhu LP, Hu SQ and Huang R (2019) Three-dimensional reverse-time migration of teleseismic receiver functions using the phase-shift-plus-interpolation method. *Geophys J Int* **271**(2): 1047–1057
- Kan RJ, Hu HX, Zeng RS, Moonay WD and Mcevilly TV (1986) Crustal structure of Yunnan Province, people's republic of China, from seismic refraction profiles. *Science* **234**(4775): 433–437
- Kosarev G, Kind R, Sobolev SV, Yuan X, Hanka W and Oreshin S (1999) Seismic evidence for a detached Indian lithospheric mantle beneath Tibet. *Science* **283**(5406): 1306–1309
- Langston CA (1979) Structure under Mount Rainier, Washington, inferred from teleseismic body waves. *J Geophys Res* **84**(39): 4749–4762
- Li JH, Shen Y and Zhang W (2018) Three-dimensional passive-source reverse-time migration of converted waves: The method. *J Geophys Res: Solid Earth* **123**(2): 1419–1434
- Li YL, Wang CS, Dai JE, Xu GQ, Hou YL and Li XH (2015) Propagation of the deformation and growth of the Tibetan-Himalayan orogen: a review. *Earth-Sci Rev* **143**: 36–61
- Ligorria JP and Ammon CJ (1999) Iterative deconvolution and receiver-function estimation. *Bull Seismol Soc Amer* **89**(5): 1395–1400
- Lin FC, Li DZ, Clayton RW and Hollis D (2013) High-resolution 3D shallow crustal structure in Long Beach, California: Application of ambient noise tomography on a dense seismic array. *Geophysics* **78**(4): Q45–Q56
- Matrullo E, Matteis RD, Satriano C, Amoroso O and Zollo A (2013) An improved 1-D seismic velocity model for seismological studies in the Campania-Lucania region (Southern Italy). *Geophys J Int* **195**: 460–473
- Schmandt B and Clayton RW (2013) Analysis of teleseismic P waves with a 5200-station array in Long Beach, California: Evidence for an abrupt boundary to Inner Borderland rifting. *J Geophys Res* **118**: 5320–5338
- Shang XF, de Hoop MV and Van Der Hilst RD (2012) Beyond receiver functions: Passive source reverse time migration and inverse scattering of converted waves. *Geophys Res Lett* **39**: L15308
- She YY, Yao HJ, Wang WT and Liu B (2019) Characteristics of seismic wave propagation in the Binchuan region of Yunnan using a dense seismic array and large volume airgun shots. *Earthquake research in China* **33**(2): 174–185
- Sun T (2019) Study of the sedimentary and crustal structures of the Binchuan area using dense array. Master thesis, (in Chinese). Institute of Geophysics China Earthquake Administration
- Tao K, Liu TZ, Ning JY and Niu FL (2014) Estimating sedimentary and crustal structure using wavefield continuation: theory, techniques and applications. *Geophys J Int* **197**(1): 443–457
- Vinnik LP (1977) Detection of waves converted from P to SV in the mantle. *Phys Earth Planet Inter* **15**(1): 39–45
- Wang BS, Tian XF, Zhang YP, Li YL, Yang W, Zhang B, Wang WT, Yang J and Li XB (2018) Seismic signature of an untuned large-volume airgun array fired in a water reservoir. *Seismol Res Lett* **89**(3): 983–991
- Wang B, Wu GH, Su YJ, Wang BS, Ge HK, Jin MP, Yang J, Zhang QM, Li T and Liu JW (2015a) Site selection and construction process of Binchuan earthquake signal transmitting seismic station and its preliminary observational Result. *J Seismol Res* **38**(1): 1–6 (in Chinese with English abstract)
- Wang CY, Lou H, Silver PG, Zhu LP and Chang LJ (2010) Crustal structure variation along 30°N in the eastern Tibetan Plateau and its tectonic implications. *Earth Planet Sci Lett* **289**: 367–376
- Wang SJ, Liu BJ, Zhang JS, Liu BF, Duan YL, Song XH, Deng XG, Ma GJ and Zang YR (2015b) Study on the velocity structure of the crust in Southwest Yunnan of the north-south seismic belt—results from the Menghai-Gengma-Lushui deep seismic sounding profile. *Sci China Earth Sci* **58**(12): 2175–2187
- Xu Y, Koper KD, Burlacu R, Herrmann RB and Li DN (2020) A new

- uniform moment tensor catalog for Yunnan, China from January 2000 through December 2014. *Seismol Res Lett* **91**(2A): 891–900
- Xu YH, Wang BS, Wang WT, Zhang B and Sun TW (2018) Multiple seismological evidences of basin effects revealed by array of Binchuan (ABC), northwest Yunnan, China. *Earthq Sci* **31**: 281–290
- Yang HF, Duan YH, Song JH, Jiang XH, Tian XF, Yang W, Wang WT and Yang J (2020) Fine structure of the Chenghai fault zone, Yunnan, China, constrained from teleseismic travel time and ambient noise tomography. *J Geophys Res: Solid Earth* **125**: e2020JB019565
- Yang H, Duan Y, Song J, Wang W, Yang W, Tian X and Wang B (2021) Illuminating high-resolution crustal fault zones using multi-scale dense arrays and airgun source. *Earthquake Research Advances*, doi:10.19743/j.cnki.0891-4176.202101002
- Yao HJ, Beghein C and Van Der Hilst RD (2008) Surface wave array tomography in SE Tibet from ambient seismic noise and two-station analysis-II. Crustal and upper-mantle structure. *Geophys J Int* **173**(1): 205–219
- Yao HJ, Van Der Hilst RD and de Hoop MV (2006) Surface wave array tomography in SE Tibet from ambient seismic noise and two-station analysis-I. Phase velocity maps. *Geophys J Int* **166**(2): 732–744
- Yeck WL, Sheehan AF and Schulte-Pelkum V (2013) Sequential $H\text{-}\kappa$ stacking to obtain accurate crustal thicknesses beneath sedimentary basins. *Bull Seismol Soc Amer* **103**(3): 2142–2150
- Yin A and Harrison TM (2000) Geologic evolution of the Himalayan-Tibet Orogen. *Annu Rev Earth Planet Sci* **28**: 211–280
- Yu YQ, Song JG, Liu KH and Gao SS (2015) Determining crustal structure beneath seismic stations overlying a low-velocity sedimentary layer using receiver functions. *J Geophys Res* **120**: 3208–3218
- Zhang YP, Wang BS, Lin GQ, Wang WT, Yang W and Wu ZH (2020) Upper crustal velocity structure of Binchuan, Yunnan revealed by dense array local seismic tomography. *Chin J Geophys* **63**(9): 3292–3306 (in Chinese with English abstract)
- Zhou Q, Guo SM and Xiang HF (2004) Principle and method of delineation of potential seismic sources in northeastern Yunnan province. *Seismology and Geology* **26**(4): 761–771 (in Chinese with English abstract)
- Zhu LP (2000) Crustal structure across the San Andreas Fault, southern California from teleseismic converted waves. *Earth Planet Sci Lett* **179**(1): 183–190
- Zhu LP and Kanamori H (2000) Moho depth variation in southern California from teleseismic receiver functions. *J Geophys Res* **105**(B2): 2969–2980